Hydrogeology Journal (2018) 26:789–802
https://doi.org/10.1007/s10040-018-1723-4

PAPER

Land subsidence due to groundwater pumping and recharge: considering the particle-deposition effect in ground-source heat-pump engineering

Xianze Cui[1] · Quansheng Liu[2] · Chengyuan Zhang[2] · Yisheng Huang[1] · Yong Fan[1] · Hongxing Wang[3]

Received: 17 January 2017 / Accepted: 14 December 2017 / Published online: 18 January 2018

Abstract
With the rapid development and use of ground-source heat-pump (GSHP) systems in China, it has become imperative to research the effects of associated long-term pumping and recharge processes on ground deformation. During groundwater GSHP operation, small particles can be transported and deposited, or they can become detached in the grain skeleton and undergo recombination, possibly causing a change in the ground structure and characteristics. This paper presents a mathematical ground-deformation model that considers particle transportation and deposition in porous media based on the geological characteristics of a dual-structure stratum in Wuhan, eastern China. Thermal effects were taken into consideration because the GSHP technology used involves a device that uses heat from a shallow layer of the ground. The results reveal that particle deposition during the long-term pumping and recharge process has had an impact on ground deformation that has significantly increased over time. In addition, there is a strong correlation between the deformation change (%) and the amount of particle deposition. The position of the maximum deformation change is also the location where most of the particles are deposited, with the deformation change being as high as 43.3%. The analyses also show that flow of groundwater can have an effect on the ground deformation process, but the effect is very weak.

Keywords Subsidence · Ground deformation · Particle deposition · Artificial recharge · China

Introduction

Land subsidence is the geological phenomenon in which the regional ground elevation decreases as a result of compression of the soil under the effect of natural or man-made factors, and can lead to serious disasters in the process of urbanization. Land subsidence can be viewed from two aspects: the soil structure and the engineering characteristics. With respect to soil structure, factors such as soil properties, stratum structure, and consolidation state can affect the process of ground deformation (Xu et al. 2012; Burbey 2003; Shi et al. 2008; Conway 2016). While from the aspect of engineering characteristics, groundwater usage and surface loadings are the main factors that lead to land subsidence (Xu et al. 2016; Chen et al. 2003; Wang et al. 2009; Gong et al. 2009). During the exploitation of groundwater, for example, in a ground-source heat-pump (GSHP) engineering project, the pore-water pressure between soil particles will dissipate because of a decrease in water levels, possibly leading to a reduction of the effective pressure and skeleton compression, as well as narrowing of the pore channels, which ultimately results in land subsidence. At the same time, small grains and particles in the skeleton can separate from the skeleton and migrate with the water, resulting in recombination of grains and ground deformation (Bedrikovetsky et al. 2011; Chen et al. 2003; Zeitoun and Wakshal 2013).

In previous studies, physical parameters such as porosity have usually been assumed to be constant; however, in fact, they are unsteady and vary during the consolidation

✉ Xianze Cui
zexiancui1989@gmail.com

[1] College of Hydraulic & Environmental Engineering, China Three Gorges University, No. 8 University Road, Yichang 443002, China

[2] State Key Laboratory of Geomechanics and Geotechnical Engineering, Institute of Rock and Soil Mechanics, Chinese Academy of Sciences, Wuhan, China

[3] Hubei Key Laboratory of Disaster Prevention and Mitigation (China Three Gorges University), Yichang, China

deformation process. Luo et al. (2007) established a three-dimensional (3D) seepage model for deep foundation-pit dewatering engineering projects in Shanghai, China, and this model was used to simulate and predict the state change of groundwater flow in deep foundation-pit dewatering engineering projects. Chen et al. (2001) established a subsidence model with 3D groundwater flows coupled to one-dimensional (1D) nonlinear consolidation. This model was then applied to engineering projects in Suzhou (eastern China), with the hydraulic conductivity varying (reduced from 0.00101 to 0.00067 m/d) during the consolidation of soft clay (Chen et al. 2003). Liu et al. (2014) established a subsidence model with changeable hydraulic conductivity that considered internal soil changes (including physical and mechanical properties) in the process of the strata deformation caused by water pumping. In this model, the Konzeny-Carman equation was adopted to describe the relationship between permeability and porosity.

Most previous research has focused on the consolidation deformation process caused by the reduction of the water level and the effective pressure (Cui and Tang 2010; Zhang et al. 2015; Xu et al. 2008; Liu and Huang 2013). However, ground deformation processes in a GSHP engineering project will have some special features: complicated hydrothermal conditions and a particle deposition effect. Groundwater flow and heat transport will go through a periodic change in GSHP engineering projects, which may affect the process of ground deformation. In addition, the biological, physical, and chemical factors, along with various types of environmental factors (such as temperature and seepage) can generate various particles such as silica, colloid and biofilm particles, with a large size range from 0.1–100 μm, that may be transported with groundwater and become deposited in pores (Bouwer 2002; Zheng et al. 2005). In the meantime, the flow characteristics of groundwater can be affected by the changing pore structure; moreover, the process of particle deposition can influence the mechanical property of the stratum. These aspects may lead to different features of the ground deformation process in the GSHP engineering project (Liu et al. 2016a, b; Low et al. 2008; Erban et al. 2014); however, few studies have considered this process.

The main objectives of this paper are: (1) to propose a ground deformation model to represent the dual-structure stratum at Wuhan; (2) to study the change law of the ground deformation and flow parameters while considering the particle deposition effect; (3) to analyze the characteristics of the ground deformation in GSHP engineering projects.

Characteristics of the dual-structure stratum at Wuhan

Wuhan is located in the eastern edge of the Jianghan Plain and on the banks of the Yangtze River (Fig. 1). Wuhan is covered with Quaternary loose sediments and is considered to be a typical dual-structure stratum (Fig. 2). In other words, the upper part is an aquitard layer with a relatively low permeability, while the lower part is a confined aquifer layer with a high permeability. This dual-structure stratum is distributed widely in the Wuchang, Hankou and Hanyang riverside areas, i.e., the first terrace of the banks of the Yangtze River and the Hanjiang River (Li 2010).

According to the particular geological structure and distribution of the groundwater, the stratum structure of the typical dual stratum in Wuhan can be divided into two groups.

1. *Phreatic layer of muddy soil and clay*. This layer has a low permeability and can be regarded as a confining bed.
2. *Confined aquifer layer of medium-coarse or coarse sand*. This layer has a high permeability and is always regarded as an aquifer.

In addition, the intermediate layer, which has permeability between the phreatic layer and the confined aquifer layer, is classified separately in places. This layer is mainly comprised of silty-fine sand in the Wuhan area; thus, it can also be regarded as an aquitard.

Methodology

Flow equation

The GSHP engineering system has two notable features: one feature is high-intensity pumping, which can cause a sharp decrease in the groundwater level; the other feature is the borehole filter that is placed in the confined aquifer layers that have high permeability. Thus, it is difficult to form a uniform groundwater head in the aquifers of a dual-structure stratum. In fact, the groundwater flow is mainly horizontal in the confined aquifer layer and vertical in the phreatic layer, and they each have an independent groundwater head.

The flow equation of the confined aquifer layer can be described as follows (Hochmuth and Sunada 1985; Li et al. 2012; Rupp and Selker 2006; Serrano and Workman 1998; Serrano 1995; Xu and Yu 2008):

$$\frac{\partial}{\partial x}\left(KM\frac{\partial H}{\partial x}\right)+\frac{\partial}{\partial y}\left(KM\frac{\partial H}{\partial y}\right)+\frac{\partial}{\partial z}\left(KM\frac{\partial H}{\partial z}\right)+w=\mu^{*}\frac{\partial H}{\partial t} \quad (1)$$

where K is hydraulic conductivity of the confined aquifer layer, M is the thickness of the confined aquifer layer, H is the groundwater head of the confined aquifer layer, w is the leakage recharge, μ^* is the storage coefficient of the confined aquifer layer. All mathematical terms used in this paper are also given in the Appendix.

Fig. 1 Study area

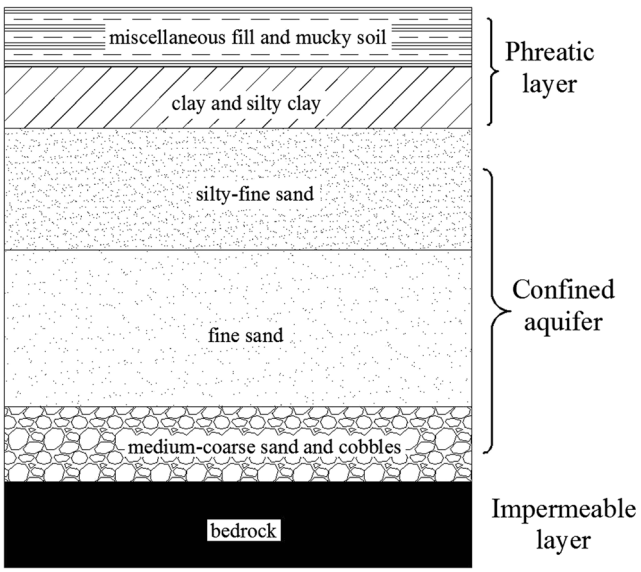

Fig. 2 Lithologic column of typical strata in Wuhan

Equation (1) can be transformed into Eq. (2) to consider both skeleton compression and the thermodynamic effect (Bo et al. 2001; Zhang et al. 2006):

$$\frac{\partial}{\partial x}\left(KM\frac{\partial H}{\partial x}\right)+\frac{\partial}{\partial y}\left(KM\frac{\partial H}{\partial y}\right)+\frac{\partial}{\partial z}\left(KM\frac{\partial H}{\partial z}\right)+w = \rho_w g(\alpha+n\beta)M\frac{\partial H}{\partial t}+n\beta_T M\frac{\partial T}{\partial t} \quad (2)$$

where ρ_w is the density of water, g is the acceleration of gravity, α is the volume compression coefficient of the porous medium, n is the porosity, β is the volume compression coefficient of water, β_T is the thermal expansion coefficient of water, T is the temperature of the groundwater; the groundwater and the porous medium are assumed to be in a state of thermal equilibrium.

The initial conditions are:

$$\begin{cases} H(x,y,z,t) = H_0 \\ w(x,y,z,t) = 0 \end{cases} \quad t = 0, (x,y,z) \in D \tag{3}$$

The boundary conditions are:

$$\begin{cases} H(x,y,z,t) = H_0 & t > 0, (x,y,z) \to \infty \\ w(x,y,z,t) = Q & t > 0, (x,y,z) \in (x_0, y_0, z_0) \\ w(x,y,z,t) = \dfrac{h-H}{h-M} K' & t > 0, (x,y,z) \in D \end{cases} \tag{4}$$

where D is the area of study, H_0 is the initial groundwater head, h is the groundwater head of the phreatic layer, K' is the hydraulic conductivity of the phreatic layer.

The flow equation of the phreatic layer can be described as:

$$\frac{h-H}{h-M} K' = \mu' \frac{\partial h}{\partial t} \tag{5}$$

where μ' is the specific yield of the phreatic layer.

Equation (5) can be transformed into Eq. (6) to consider both skeleton compression and the thermodynamic effect (Bo et al. 2001; Zhang et al. 2006):

$$\frac{h-H}{h-M} K' = \rho_w g(\alpha + n\beta) M \frac{\partial h}{\partial t} + n\beta_T M \frac{\partial T}{\partial t} \tag{6}$$

The initial conditions are:

$$\begin{cases} H(x,y,z,t) = H_0 \\ h(x,y,z,t) = H_0 \end{cases} \quad t = 0, (x,y,z) \in D \tag{7}$$

The boundary conditions are:

$$\begin{cases} H(x,y,z,t) = H_0 \\ h(x,y,z,t) = H_0 \end{cases} \quad t > 0, (x,y,z) \to \infty \tag{8}$$

Thermal transport equation

There are four main factors that can influence heat transport in porous media:

1. Thermal advection, i.e., heat transfer as a result of the flow of the pore fluid
2. Thermal conduction, i.e., heat transfer as a result of temperature gradients
3. Thermal dispersion, i.e., heat transfer as a result of non-uniform velocities of the solute
4. Source-sink term

Based on these factors, a thermal transport equation that considers the particle transportation and deposition process can be obtained (Wang et al. 2012).

Thermal advection

Heat difference between the inflow and outflow of the element (hexahedron mini-element model) via thermal advection per unit time can be described as (Bergman and Incropera 2011)

$$\begin{cases} [C_w T v_x(x,y,z) - C_w T v_x(x+\Delta x, y, z)] dydzdt = -\dfrac{\partial}{\partial x}(C_w T v_x) dxdydzdt \\ [C_w T v_y(x,y,z) - C_w T v_y(x, y+\Delta y, z)] dxdzdt = -\dfrac{\partial}{\partial y}(C_w T v_y) dxdydzdt \\ [C_w T v_z(x,y,z) - C_w T v_z(x, y, z+\Delta z)] dxdydt = -\dfrac{\partial}{\partial z}(C_w T v_z) dxdydzdt \end{cases} \tag{9}$$

where v_x, v_y, v_z are components of Darcy velocity in x, y, z directions respectively, C_w is the volumetric thermal capacity of groundwater, T is temperature.

The total heat difference between the inflow and outflow of the groundwater of the element via thermal advection per unit time can be expressed as:

$$-\mathrm{div}(C_w T v) dxdydzdt \tag{10}$$

Thermal conduction

Fourier's law states that the heat flux through a material is proportional to the negative gradient of the temperature that the heat transverses. Thus, the heat flux via thermal conduction can be expressed as:

$$I_T = -\lambda_T \mathrm{grad} T \tag{11}$$

where λ_T is heat conductivity of bulk porous media.

Thermal dispersion

The hydrodynamic dispersion coefficient can express the diffusion capacity of a substance to porous media under a specified flow rate, and it includes the effects of both diffusion and pore-scale groundwater velocity variations. It reflects the effects of both groundwater flow and pore structure on the transportation of a solute on a macro-scale. Mechanical dispersion includes longitudinal and lateral dispersion, representing the dispersion phenomenon along and perpendicular to the flow direction, respectively. Thermal dispersion can both enhance viscous dissipation and intensify the heat diffusion in porous media.

The heat flux of thermal dispersion can be described as:

$$I_D = -\lambda_D \mathrm{grad} T \tag{12}$$

$$\lambda_D = C_w g \alpha_0 |v| \tag{13}$$

where λ_D is the thermal mechanical dispersion coefficient, α_0 is thermal dispersity.

The heat flux per unit area via thermal dispersion can be described as:

$$I = I_T + I_D = -(\lambda_T + \lambda_D)\mathrm{grad}T \tag{14}$$

$$\lambda = \lambda_T + \lambda_D \tag{15}$$

where λ is the thermodynamic dispersion coefficient.

The heat difference between the inflow and outflow of the element via thermal conduction and mechanical dispersion per unit time can be described as:

$$\begin{cases} [I_x(x,y,z) - I_x(x+\Delta x,y,z)]dydzdt = -\dfrac{\partial I_x}{\partial x}dxdydzdt \\ [I_y(x,y,z) - I_y(x,y+\Delta y,z)]dxdzdt = -\dfrac{\partial I_y}{\partial y}dxdydzdt \\ [I_z(x,y,z) - I_z(x,y,z+\Delta z)]dxdydt = -\dfrac{\partial I_z}{\partial z}dxdydzdt \end{cases} \tag{16}$$

The total heat difference between the inflow and outflow of groundwater of the element via thermal conduction and mechanical dispersion per unit time can be expressed as:

$$-\mathrm{div}(I)dxdydzdt \tag{17}$$

Source-sink term

The heat flux of the inflow and outflow of groundwater in the system as well as the source-sink term can be described as:

$$qC_wT^*dxdydzdt \tag{18}$$

where q is the volume flux of the source, T^* is the temperature of the source.

Thermal transport equation

Heat changes caused by changes of temperature in an element per unit time are given by:

$$C_a\frac{\partial T}{\partial t}dxdydzdt \tag{19}$$

where C_a is the volume heat capacity of the aquifer.

The heat difference between the inflow and outflow result in the change of heat in the element; thus, the following can be deduced based on the law of conservation of energy:

$$C_a\frac{\partial T}{\partial t} = \mathrm{div}(\lambda \mathrm{grad}T) - \mathrm{div}(C_wTv) + qC_wT^* \tag{20}$$

Thus, it can be concluded that:

$$[nC_w + (1-n)C_r]\frac{\partial T}{\partial t} = \mathrm{div}\{[\lambda_D + n\lambda_w + (1-n)\lambda_r]\mathrm{grad}T\} - \mathrm{div}(C_wTv) + qC_wT^* \tag{21}$$

where C_a, C_w, C_r are heat capacities of the bulk porous medium, water and soil skeleton respectively, λ_D is the thermal mechanical dispersion coefficient of the porous media, λ_w, λ_r are heat conduction coefficients of the water and soil skeleton respectively, v is Darcy velocity.

Based on the law of particle deposition, the relationship between the porosity and the deposition mass of particles can be expressed as (Liu et al. 2016a, b):

$$n = \frac{\rho_s n_i - S}{\rho_s + C} \tag{22}$$

where ρ_s is the density of the suspended particles, n_i is the initial porosity, S is the concentration of particles deposited in pores, C is the concentration of suspended particles.

Thus, it can be concluded that:

$$\left[\frac{\rho_s n_i - S}{\rho_s + C}C_w + \frac{\rho_s(1-n_i) + C + S}{\rho_s + C}C_r\right]\frac{\partial T}{\partial t} = \mathrm{div}\left\{\left[\lambda_D + \frac{\rho_s n_i - S}{\rho_s + C}\lambda_w + \frac{\rho_s(1-n_i) + C + S}{\rho_s + C}\lambda_r\right]\mathrm{grad}T\right\} - \mathrm{div}(C_wTv) + qC_wT^* \tag{23}$$

For particles at low concentration ($\rho_s \gg C$), Eq. (23) can be simplified to:

$$\left[\left(n_i - \frac{S}{\rho_s}\right)C_w + \left(1 - n_i + \frac{S}{\rho_s}\right)C_r\right]\frac{\partial T}{\partial t} = \mathrm{div}\left\{\left[\lambda_D + \left(n_i - \frac{S}{\rho_s}\right)\lambda_w + \left(1 - n_i + \frac{S}{\rho_s}\right)\lambda_r\right]\mathrm{grad}T\right\} - \mathrm{div}(C_wTv) + qC_wT^* \tag{24}$$

This is the thermal transport equation of the aquifer that considers the particle deposition process.

Settlement analysis

The storage coefficient can be calculated as:

$$\mu^* = \mu_s M = \rho_w g(\alpha + n\beta)M \tag{25}$$

where μ^* is the storage coefficient, μ_s is the specific storage, ρ_w is the water density, n is the porosity, β is the water volume compressibility, α is the solid volume compressibility.

For particles at low concentration ($\rho_s \gg C$), the relationship between the porosity and the deposition mass of particles can be described as (Liu et al. 2016a, b):

$$n = n_i - \frac{S}{\rho_s} \tag{26}$$

According to the Kozeny-Carman equation (Xu et al. 2008), the permeability is given by:

$$k = \frac{n^3}{c(1-n)^2 s^2} \tag{27}$$

where c and s denote the Kozeny constant and specific surface area based on the solid volume, respectively.

Thus, the hydraulic conductivity can be expressed as:

$$K = \frac{\rho_w g k}{\mu} = \frac{\rho_w g n^3}{c s^2 \mu (1-n)^2} \tag{28}$$

According to the features of aquifer compressibility:

$$\alpha = 0.434 \frac{(1-n) C_C}{\sigma'} \tag{29}$$

where C_C is the compression index, σ' is effective stress.

The flow equation of the confined aquifer layer can be described as:

$$\frac{\partial}{\partial x}\left[M \frac{\rho_w g n^3}{c s^2 \mu (1-n)^2} \frac{\partial H}{\partial x}\right] + \frac{\partial}{\partial y}\left[M \frac{\rho_w g n^3}{c s^2 \mu (1-n)^2} \frac{\partial H}{\partial y}\right] + \frac{\partial}{\partial z}\left[M \frac{\rho_w g n^3}{c s^2 \mu (1-n)^2} \frac{\partial H}{\partial z}\right] + w = \rho_w g M \left[0.434 \frac{(1-n) C_C}{\sigma'} + \left(n_i - \frac{S}{\rho_s}\right)\beta\right] \frac{\partial H}{\partial t} + \left(n_i - \frac{S}{\rho_s}\right) \beta_T M \frac{\partial T}{\partial t} \tag{30}$$

where w is given by:

$$w = \frac{h-H}{h-M} K' = \frac{h-H}{h-M} \frac{\rho_w g n'^3}{c s^2 \mu (1-n')^2} \tag{31}$$

Substituting Eq. (31) into Eq. (30):

$$\frac{\partial}{\partial x}\left[\frac{M n^3}{c s^2 \mu (1-n)^2} \frac{\partial H}{\partial x}\right] + \frac{\partial}{\partial y}\left[\frac{M n^3}{c s^2 \mu (1-n)^2} \frac{\partial H}{\partial y}\right] + \frac{\partial}{\partial z}\left[M \frac{\rho_w g n^3}{c s^2 \mu (1-n)^2} \frac{\partial H}{\partial z}\right] + \frac{n'^3 (h-H)}{c s^2 \mu (1-n')^2 (h-M)} = \rho_w g M \left[0.434 \frac{(1-n) C_C}{\sigma'} + \left(n_i - \frac{S}{\rho_s}\right)\beta\right] \frac{\partial H}{\partial t} + \left(n_i - \frac{S}{\rho_s}\right) \beta_T M \frac{\partial T}{\partial t} \tag{32}$$

Ignoring the compressibility of water ($\beta = 0$):

$$\frac{\partial}{\partial x}\left[\frac{M n^3}{c s^2 \mu (1-n)^2} \frac{\partial H}{\partial x}\right] + \frac{\partial}{\partial y}\left[\frac{M n^3}{c s^2 \mu (1-n)^2} \frac{\partial H}{\partial y}\right] + \frac{\partial}{\partial z}\left[M \frac{\rho_w g n^3}{c s^2 \mu (1-n)^2} \frac{\partial H}{\partial z}\right] + \frac{n'^3 (h-H)}{c s^2 \mu (1-n')^2 (h-M)} = \rho_w g M \left[0.434 \frac{(1-n) C_C}{\sigma}\right]' \frac{\partial H}{\partial t} + \left(n_i - \frac{S}{\rho_s}\right) \beta_T M \frac{\partial T}{\partial t} \tag{33}$$

The flow equation of the phreatic layer can be described as:

$$\frac{h-H}{h-M} \frac{n'^3}{c s^2 \mu (1-n')^2} = \rho_w g M \left[0.434 \frac{(1-n) C_C}{\sigma}' + \left(n_i - \frac{S}{\rho_s}\right)\beta\right] \frac{\partial h}{\partial t} + \left(n_i - \frac{S}{\rho_s}\right) \beta_T M \frac{\partial T}{\partial t} \tag{34}$$

Ignoring the compressibility of water ($\beta = 0$):

$$\frac{n'^3 (h-H)}{c s^2 \mu (1-n')^2 (h-M)} = \rho_w g M \left[0.434 \frac{(1-n) C_C}{\sigma}\right]' \frac{\partial H}{\partial t} + \left(n_i - \frac{S}{\rho_s}\right) \beta_T M \frac{\partial T}{\partial t} \tag{35}$$

Ground deformations caused by pumping and injection consist of deformations of the phreatic layer and the confined aquifer layer, that is:

$$S_T = S_1 + S_2 \tag{36}$$

where S_T is the total deformation of the ground, S_1, S_2 are deformations of the phreatic layer and the confined aquifer layer, respectively, and are given by:

$$S_1 = M_{S_1} \frac{(H_0 - H_1) \gamma_w m}{2 E_S} \tag{37}$$

$$S_2 = M_{S_2} \sum_{i=1}^{n} \left(\Delta \sigma_{Si} \frac{m_i}{E_{Si}}\right) \tag{38}$$

where M_{S_1} and M_{S_2} are empirical coefficients of the settlement, H_0 is the initial water head of the confined aquifer layer, H_1 is the water head of the confined aquifer after extraction, γ_w is the unit weight of water, m is the thickness of the phreatic layer, E_S and E_{Si} are the compression modulus of the phreatic layer and the confined aquifer layer, respectively, $\Delta\sigma_{Si}$ is the effective stress increment of each layer, m_i is the thickness of each layer.

In this manner, the ground deformation can be calculated according to the relationship between the water head and the change of the effective stress, combining Eqs. (24), (33) and (35) into (38) using a second-development of COMSOL Multiphysics. COMSOL Multiphysics is a universal engineering software based on finite-element analysis, which has a large set of functions for analyses and solutions, and provided a second-development interface at different levels. In this study, the mathematical model was solved through a modification of the built-in functions, which mainly includes Darcy's law and the Biot poroelasticity constitutive model.

Study area

Engineering background

The Baibuting Garden community adopted GSHP technology for the heating and cooling of buildings. The

GSHP system consists of three pumping wells and three recharge wells, and the pumping rate is 110 m^3/h (both for the withdrawal wells and the recharge wells). The wells are 47 m deep, and 0.15 m wide in diameter. The well group is distributed in a region of 80 m × 80 m, as shown in Fig. 3.

Geological condition

According to the geotechnical investigation on Baibuting Garden, the upper layer is mainly a soft plastic silty clay of Quaternary Holocene, the middle layer is a dense silty sand of Quaternary Holocene, and the lower layer is siltstone and pelitic siltstone of Silurian. The strata distributions are listed in Table 1.

To obtain the initial temperature distribution of the groundwater, two test wells were drilled near W1 and W2. The results of the groundwater temperature investigation at various depths and times are shown in Figs. 4 and 5. Figure 4 shows that the groundwater temperature increases slowly (it is almost constant) as depth increases below the depth of 10 m, whereas Fig. 5 illustrates the change law of the groundwater temperature over depth to 30 m at different times, and it shows that the effect of surface temperature can reach the depth of approximately 20 m, below which the temperature tends to be stable. The figure shows that the changes of surface temperature mainly affect the regions of the ground above 20-m depth. In other words, the temperature below 20-m depth can be regarded as constant. Based on this observation, the groundwater temperature was chosen to be 18 °C in this study area.

The engineering site lies in the first terrace of the Yangtze River, and the groundwater is greatly affected by the river. Because of seasonal variation in the water level of Yangtze River, the groundwater flow will change over time; thus, it is advisable to study the effects of groundwater flow. Three modes are considered in this study, i.e., reverse flow, forward flow and cross flow, as shown in Fig. 6. In this study, the flow rate is 3×10^{-6} m/s (100 m/year).

Operational mode

In this study, the operational process of the GSHP is simplified to four steps in a cycle. The heating and cooling periods are both 90 d; between these periods, there is a 90-d inoperational period. For well flushing, the following two modes were chosen:

Continuous mode. Run continuously for 2 years, set W1, W2 and W3 as the pumping wells and W4, W5 and W6 as the recharge wells.

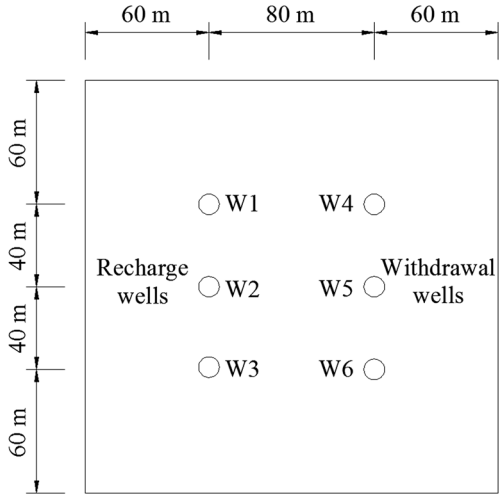

Fig. 3 Spatial distribution of the well group

Flushing mode. The same as the continuous mode in the first year, and then the pumping and recharge wells were swapped in the second year.

Parameters

To simplify the computation, similar layers are merged. Generally, these lithologic layers can be divided into the phreatic layer and the confined aquifer layer. More narrowly, the miscellaneous fill layer and clay layer can be classified as the phreatic layer, and the fine sand layer can be classified as the confined aquifer layer. The geological parameters of each layer are presented in Table 2. The temperature of the recharge water in summer and winter are 30 and 5 °C, respectively.

Results

Different recharge volumes

To study the deformation law of the ground for different recharge volumes, three modes (i.e., no recharge, half recharge and total recharge) are calculated. Figure 7 shows the ground deformation for different recharge volumes on day 90, and the ground deformation data were collected on the east–west axis shown in Fig. 3. Figure 8 shows the deformation law of the central point for different recharge volumes during a whole year.

Figures 7 and 8 show that maximum deformation was located near the pumping well and was severely affected by the recharge volume. The settlement reached 96 mm near the pumping well for the no recharge condition, whereas for the total recharge condition it was only 60 mm. The deformation decreases as the recharge

Table 1 The distribution of soil layers

Strata serial No.	Name of soil layer	Cover depth (m)	Layer thickness (m)	Main characteristics
1	Miscellaneous fill	0	0.60–4.20	Wet and loose state
2	Plain fill	0.60–4.20	0.50–5.30	Mainly cohesive soil, discontinuous
3	Clay	1.10–5.62	1.00–7.10	Contains organic matter, saturated, plastic
4	Silty clay	2.31–8.91	0.50–6.70	Saturated, soft plastic
5	Silt	4.85–11.92	1.00–3.50	Contains mica, saturated, slightly dense
6	Silty clay	5.62–13.25	0.80–6.30	Horizontal bedding, soft plastic
7	Muddy-silty clay	7.15–15.34	0.90–5.10	Saturated, fluidal plastic
8	Silt	9.58–18.19	0.50–5.20	Saturated, medial density, low toughness
9	Silty sand	11.22–21.05	0.80–6.30	Contains mica, saturated, slightly dense
10	Silty sand	12.11–24.54	2.56–22.11	Contains mica, continuous distribution
11	Coarse sand	36.58–45.22	1.45–2.45	Saturated, dense, contains 5–10% gravel
12	Silty clay	38.12–47.15	0.7–3.70	Saturated, plastic
13	Cobble	39.50–49.22	0.5–1.6	Contains 50–60% cobbles (3–8 cm)
14	Pelitic siltstone	41.22–50.14	2.5–11.7	Soft rock

volume increases; it can even uplift the ground by up to 29 mm for the total recharge mode. Figure 8 also shows that land subsidence has a periodic change rule for the pumping and injection process for a year, i.e., the ground deformation is similar during the heating and cooling periods. During the two inoperational periods, the ground deformation is almost the same. In addition, during the inoperational period, the land subsidence at the central point is approximately 21.5 mm, and this value is minimally affected by the recharge volume.

Different operational modes

To study the ground deformation law for different operational modes, the continuous mode and flushing mode are calculated; the result is illustrated in Fig. 9. The ground deformation data were collected on the east–west axis shown in Fig. 3. It is obvious that the ground deformation is significantly influenced by the operational mode. The ground deformation law is very different for the two operational modes—for example, the largest ground settlement site is near −40 and +40 m for the continuous mode and flushing mode, respectively; however, the maximum settlement value changes from 77.6 to 77.8 mm, i.e., it was almost unchanged.

Different flow modes

To study the ground deformation law for different flow modes, four flow modes—no flow, forward flow, reverse flow

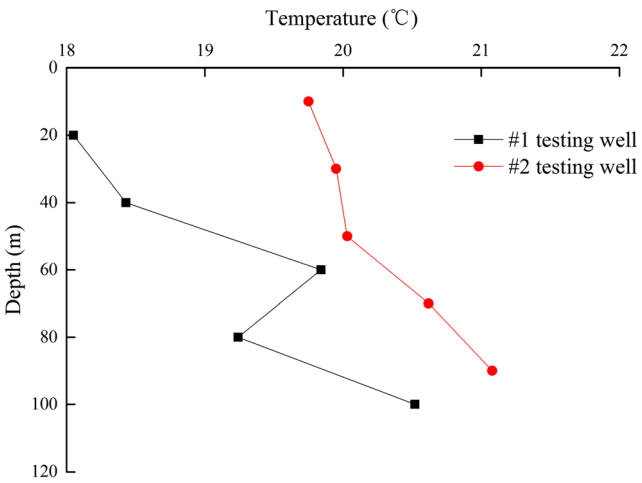

Fig. 4 Initial temperature of the groundwater

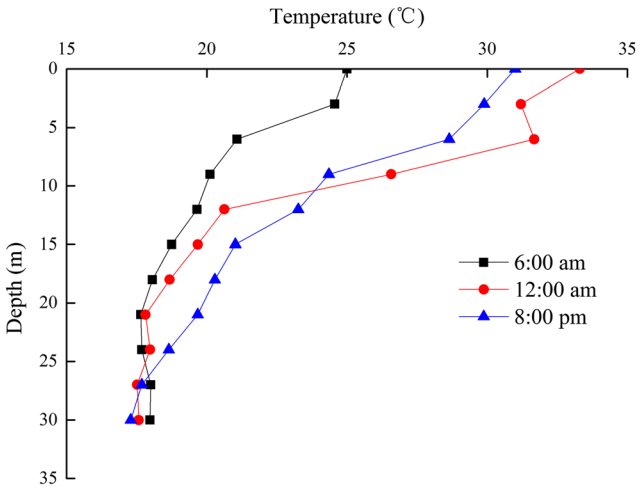

Fig. 5 Groundwater temperature-depth profiles as a function of time (No. 1 testing well)

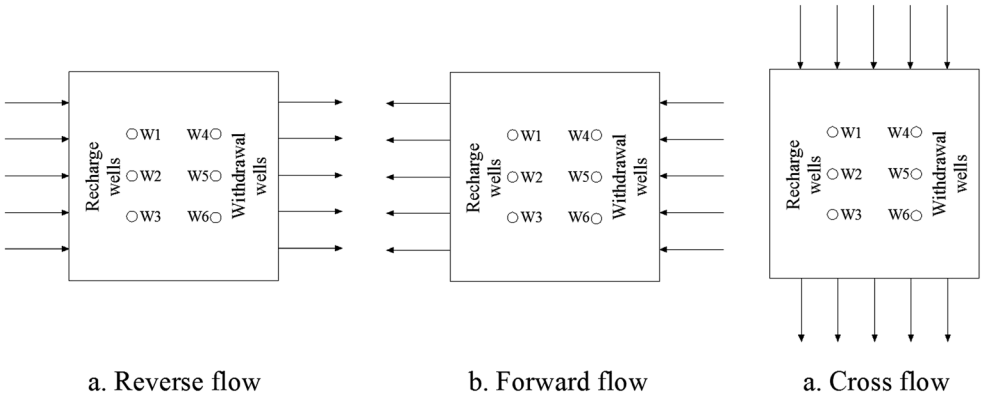

Fig. 6 Flow modes of groundwater: a. reverse flow, b. forward flow, c. cross flow

and cross flow—were considered, the result of which is illustrated in Fig. 10. The ground deformation data were also collected on the east–west axis shown in Fig. 3. The results show that ground deformation is barely affected by the groundwater flow in the GSHP operation stage. In other words, the initial background groundwater flow regime has little effect on the ground deformation during the operational stage. Consequently, the effect of groundwater flow during the operational stage can be neglected.

Considering particle deposition

The ground deformation and deformation change (%) after operation for two cycles for the continuous mode are illustrated in Figs. 11 and 12, respectively, and the ground deformation data were also collected on the east–west axis shown in Fig. 3. Deformation change (%) is defined as follows:

$$Deformation\ change(\%) = \frac{S_{nd} - S_{cd}}{S_{nd}} \times 100\% \quad (39)$$

where S_{nd} is the ground settlement that neglects the particle deposition effect, S_{cd} is the ground settlement that considers the particle deposition effect.

Figure 11 shows that the particle deposition process has an effect on the deformation of the ground, and the effect will significantly increase as time increases. The results showed that the maximum ground settlement near the pumping well is 77.6 mm when the particle deposition effect is neglected. When the particle deposition is considered, this value is 76.0 mm on day 90, 75.3 mm on day 270 and 69.4 mm on day 630. Figure 12 shows that the maximum deformation change (%) is distributed over an area (x) of 30–40 m. In addition, the curves of the deformation change (%) are highly related to the curves of the particle deposition, and the position of maximum change (%) is also the location where most particles are deposited. The deformation change (%) at this position is as high as 43.3%.

The ground deformation law for the continuous mode during the shut-off period is illustrated in Figs. 13 and 14, and the ground deformation data were also collected on

Table 2 Geological parameter

Parameter	Unit	Miscellaneous fill	Clay	Fine sand	Pelitic siltstone
Layer thickness	m	4	15	26	5
Porosity	–	0.5	0.5	0.35	0.1
Permeability	m^2	1×10^{-11}	5×10^{-13}	5×10^{-11}	5×10^{-15}
Dry density	kg/m^3	2,100	2,200	2,600	2,600
Poisson's ratio	–	0.4	0.35	0.3	0.2
Young's modulus	Pa	2×10^6	5×10^6	4×10^7	1×10^9
Thermal conductivity	W/(m·°C)	1.4	1.2	1.8	2.2
Specific heat capacity	J/(kg·°C)	800	1,200	2,000	1,600

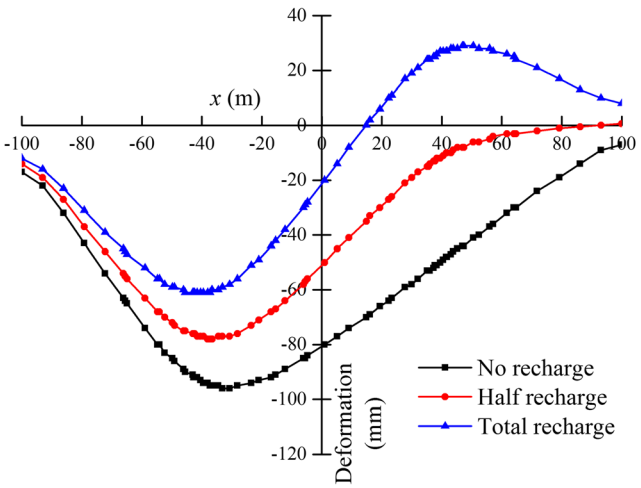

Fig. 7 Ground deformation for different recharge scenarios on the east–west axis (day 90)

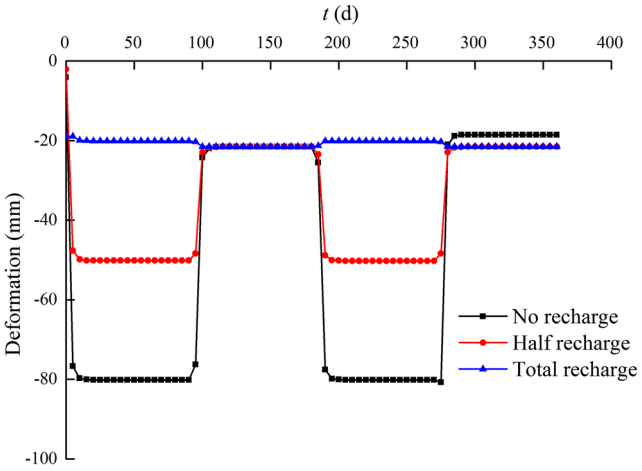

Fig. 8 Deformation versus time for different recharge scenarios (in central point)

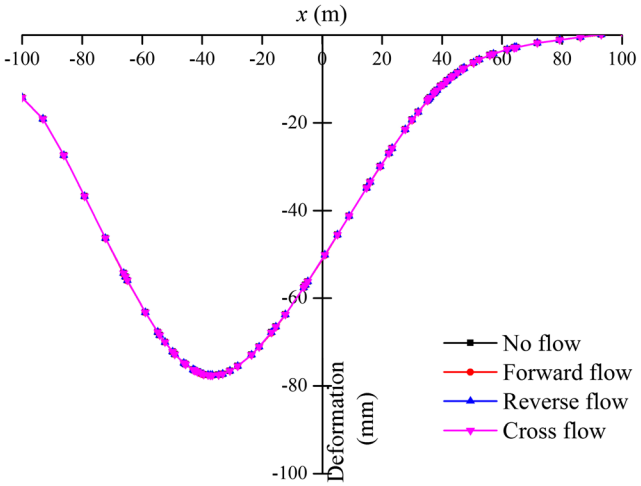

Fig. 10 Ground deformation under different flow modes on the east–west axis (day 90)

the east–west axis shown in Fig. 3. Figure 13 shows that the particle deposition process has some influence on the deformation of the ground during the shut-off period. The maximum ground deformation of 21.5 mm is at the center when the effect of particle concentration is neglected. When the deposition effect is considered, the position of the maximum ground deformation moves to $x = -4.8$ m, and ground deformation at the center is relatively small due to particle deposition. Additionally, based on Fig. 14, the curves of the deformation change (%) are highly related to the curves of particle deposition.

The ground deformation law for the flushing mode on days 450 and 630 are illustrated in Figs. 15 and 16, respectively, and the ground deformation data were also collected on the east–west axis shown in Fig. 3. The maximum ground deformation lies near the pumping well, i.e., at $x = -40$ m (Fig. 15). The particle deposition quantity in the stratum is greatly reduced because of well flushing compared with the previous year. This change in particle deposition quantity leads to a slight change in ground deformation during days 450–630, and the maximum deformation change (%) changes from 6.7 to 9.1%. Figure 16 shows that the maximum deformation change (%) is distributed around $x = 5.2$ m, which is the location where the most particles are deposited.

A study on the effect of the groundwater flow in the GSHP operation stage has been discussed in the previous section; thus, its influence in the shut-off stage is discussed in this section. The ground deformation and the deformation change (%) during the shut-off period for different flow modes are illustrated in Figs. 17 and 18, respectively, and the ground deformation data were also collected on the east–west axis shown in Fig. 3.

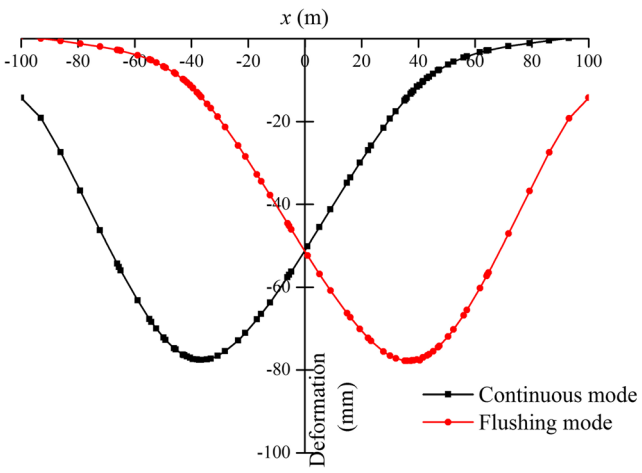

Fig. 9 Ground deformation under different operational modes on the east–west axis (day 450)

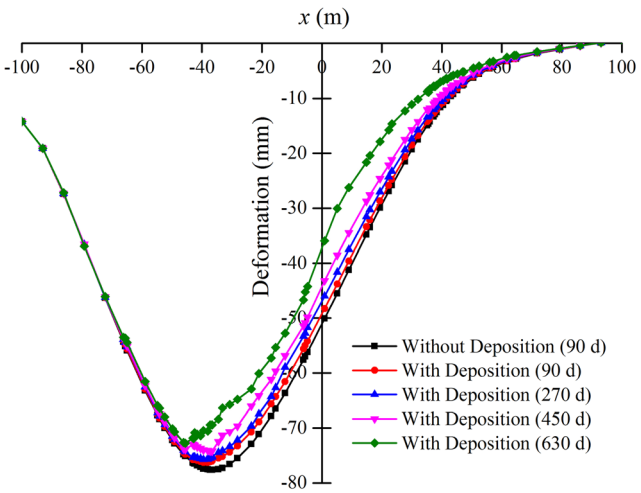

Fig. 11 Ground deformation under continuous mode on the east–west axis

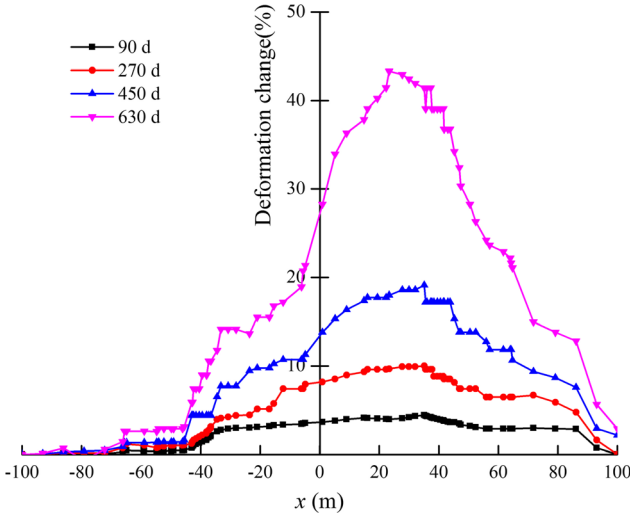

Fig. 12 Deformation change (%) under continuous mode on the east–west axis (with deposition)

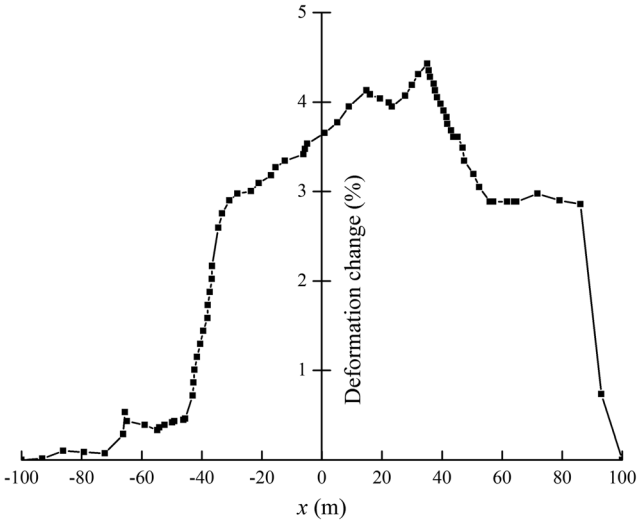

Fig. 14 Deformation change (%) under continuous mode on the east–west axis at day 180

The results show that the flow mode of the groundwater can have an effect on the ground deformation, but the effect is very weak. For the condition of forward flow, the ground deformation near the pumping well decreases, whereas near the recharge well, the value increases, due to the transport of particles towards the pumping wells. In contrast, the ground deformation near the pumping well increases, and that near the recharge well decreases for the reverse flow; this behavior can be attributed to particle transport towards the recharge wells. The ground deformation law for cross flow is similar to that for reverse flow, i.e., the ground deformation near the pumping well increases, whereas near the recharge well, the value decreases. It is concluded that the particle concentration in the central area is relatively high; thus, particles may migrate under the effects of groundwater scouring. Overall, the effect of groundwater flow on the ground deformation is relatively small.

Conclusions

In this paper, a ground deformation model that considers the characteristics of a GSHP engineering project and the effect of particle deposition was proposed for the dual-structure stratum in Wuhan. The main conclusions are as follows.

1. Based on the characteristics of a typical dual-structure stratum in Wuhan, a ground deformation model that considers the changing porosity and declining permeability

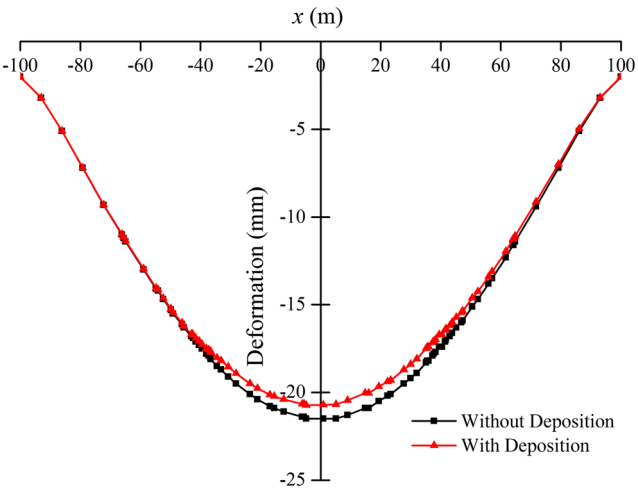

Fig. 13 Ground deformation under continuous mode on the east–west axis at day 180

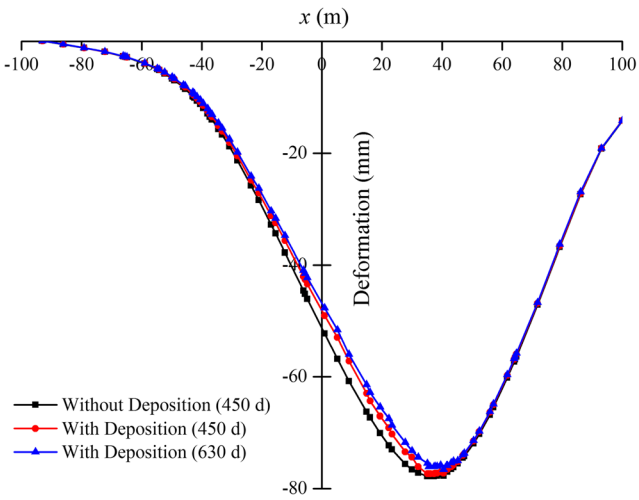

Fig. 15 Ground deformation under flushing mode on the east–west axis

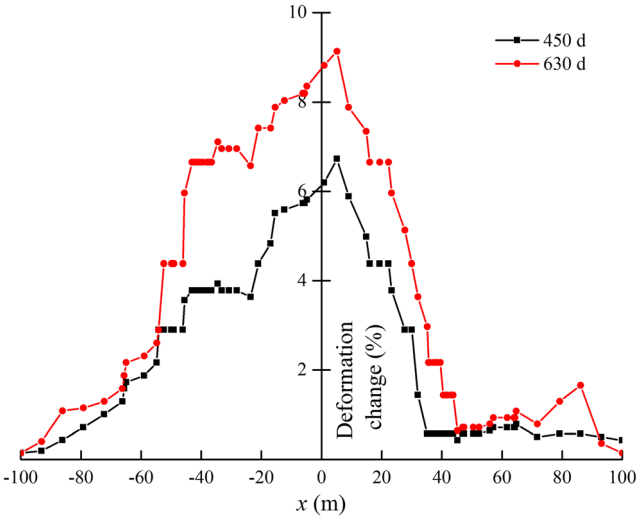

Fig. 16 Deformation change (%) under flushing mode on the east–west axis (with deposition)

caused by particle deposition in the ground was developed to determine the value of ground deformation.

2. A mathematical model of thermal transport in a confined aquifer layer was established, and the effects of thermal advection, thermal conduction and thermal dispersion were considered. In addition, the effects of particle deposition on the formation parameters were also considered in the thermal transport equation.
3. Particle deposition during the long-term pumping and recharge process has an effect on the deformation of the ground, with the effect significantly increasing over time. The curves of the deformation change (%) are highly related to the curves of particle deposition. Moreover, different flow modes of the groundwater can have an effect on ground deformation, but the effect is very weak.

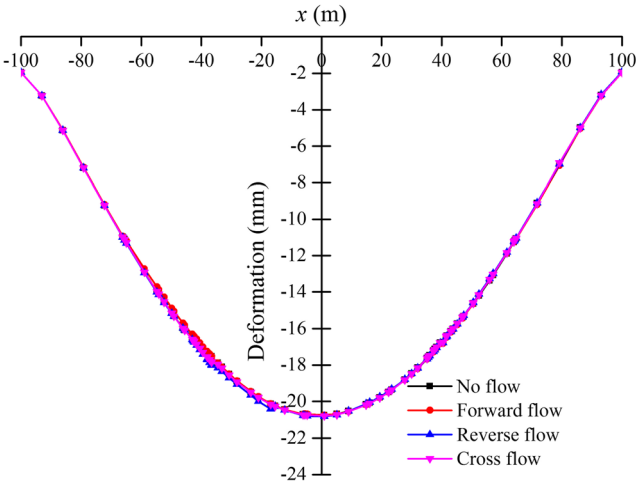

Fig. 17 Ground deformation under different flow modes on the east–west axis (day 180)

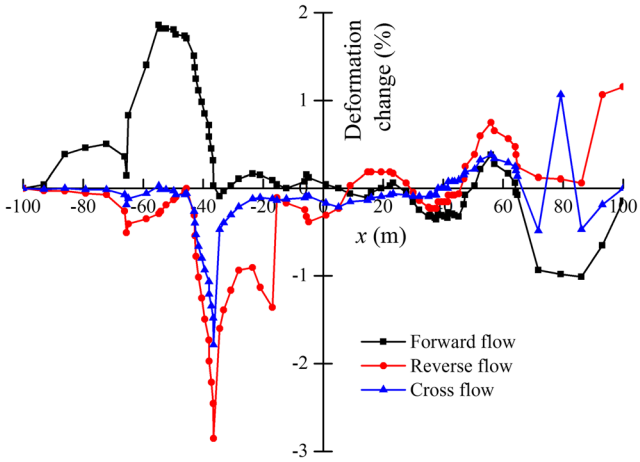

Fig. 18 Deformation change (%) under different flow modes on the east–west axis (day 180)

Funding Information This research was supported by the National Natural Science Foundation of China (Grant no. 41702254, 51609127) and Hubei Provincial Natural Science Foundation of China (Grant no. 2015CFB545, 2016CFB237).

Appendix 1: nomenclature

Latin symbols:

c	Kozeny constant
C	Concentration of suspended particles
C_a, C_w, C_r	Heat capacity of bulk porous medium, water and soil skeleton
C_C	Compression index
D	Area of study
E_S, E_{Si}	Compression modulus of phreatic layer and confined aquifer layer
g	Acceleration of gravity
h	Groundwater head of phreatic layer
H	Groundwater head of confined aquifer layer
H_0	Initial groundwater head
H_1	Water head of confined aquifer after extraction
K	Hydraulic conductivity of confined aquifer layer
K'	Hydraulic conductivity of phreatic layer
m	Thickness of phreatic layer
m_i	Thickness of each layer
M	Thickness of confined aquifer layer
M_{S_1}, M_{S_2}	Empirical coefficient of settlement
n	Porosity
n_i	Initial porosity
q	Volume flux of source
s	Specific surface area based on the solid volume
S	Concentration of particles deposited in pores
S_1, S_2	Deformations of phreatic layer and confined aquifer layer
S_T	Total deformation of ground
S_{nd}	

	Ground settlement which neglects particle deposition effect
S_{cd}	Ground settlement considering particle deposition effect
T	Temperature of groundwater
T^*	Temperature of source
v	Flow rate of groundwater
v_x, v_y, v_z	Flow velocity in x, y, z directions

Greek symbols:

α	Volume compression coefficient of porous medium
α_0	Thermal dispersity
β	Volume compression coefficient of water
β_T	Thermal expansion coefficient of water
λ	Thermodynamic dispersion coefficient
λ_D	Thermal mechanical dispersion coefficient
λ_T	Heat conductivity of bulk porous media
λ_w,	Heat conduction coefficient of water and soil
λ_r	skeleton
μ'	Specific yield of phreatic layer
μ^*	Storage coefficient of confined aquifer layer
μ_s	Specific storage
ρ_s	Density of suspended particles
ρ_w	Density of water
σ'	Effective stress
$\Delta\sigma_{Si}$	Effective stress increment of each layer
w	Leakage recharge

References

Bedrikovetsky P, Siqueira FD, Furtado CA, Souza ALS (2011) Modified particle detachment model for colloidal transport in porous media. Transp Porous Media 86(2):353–383

Bergman TL, Incropera FP (2011).Fundamentals of heat and mass transfer. Wiley, Chichester, UK

Bo C, Ning L, Ruihua Z (2001) Finite element analysis of fully coupled thermo-hydro-mechanic behavior of porous media (in Chinese). Chin J Rock Mech Eng 20(4):467–472

Bouwer H (2002) Artificial recharge of groundwater: hydrogeology and engineering. Hydrogeol J 10(1):121–142

Burbey TJ (2003) Use of time-subsidence data during pumping to characterize specific storage and hydraulic conductivity of semi-confining units. J Hydrol 281(1):3–22

Chen CX, Yuan SP, Wang BH (2001) Research on groundwater exploitation: land subsidence model (in Chinese). Hydrogeol Eng Geol 28(2):5–8

Chen C, Pei S, Jiao J (2003) Land subsidence caused by groundwater exploitation in Suzhou City, China. Hydrogeol J 11(2):275–287

Conway BD (2016) Land subsidence and earth fissures in south-central and southern Arizona, USA. Hydrogeol J 24(3):649–655

Cui ZD, Tang YQ (2010) Land subsidence and pore structure of soils caused by the high-rise building group through centrifuge model test. Eng Geol 113(1):44–52

Erban LE, Gorelick SM, Zebker HA (2014) Groundwater extraction, land subsidence, and sea-level rise in the Mekong Delta, Vietnam. Environ Res Lett 9(8):084010

Gong SL, Li C, Yang SL (2009) The microscopic characteristics of shanghai soft clay and its effect on soil body deformation and land subsidence. Environ Geol 56(6):1051–1056

Hochmuth DP, Sunada DK (1985) Ground-water model of two-phase immiscible flow in coarse material. Groundwater 23(5):617–626

Li Y (2010) Foundation pit dewatering and ground subsidence in binary structural stratum of Wuhan (in Chinese). PhD Thesis, China University of Geosciences, Wuhan, China

Liu B, Zhang G, Jiang YH (2014) Settlement research on single pumping well of foundation pit using changeable permeability coefficient model (in Chinese). Hydrogeol Eng Geol 22(6):1123–1127

Liu QS, Cui XZ, Zhang CY (2016a) Permeability reduction model of particles deposit in porous medium considering changeable porosity (in Chinese). Chin J Rock Mech Eng 35(A01):3308–3314

Liu QS, Cui XZ, Zhang CY, Huang SB (2016b) Experimental investigation of suspended particles transport through porous media: particle and grain size effect. Environ Technol 37(7):854–864

Liu Y, Huang HJ (2013) Characterization and mechanism of regional land subsidence in the Yellow River Delta, China. Nat Hazards 68(2):687–709

Li Y, He ZZ, Yan GH, Liao ZY, Liang SY (2012) Excavation dewatering and ground subsidence in dual structural stratum of Wuhan (in Chinese). Chin J Geotech Eng 34:S1

Low HE, Phoon KK, Tan TS, Leroueil S (2008) Effect of soil microstructure on the compressibility of natural Singapore marine clay. Can Geotech J 45(2):161–176

Luo ZJ, Zhang YP, Liu JB (2007) Three-dimensional seepage numerical simulation of deep foundation pit dewatering in complicated quaternary loose sediments with great thickness-a case study of dewatering reconstructed foundation pit at Dongjiadu subway of the 4th line in Shanghai (in Chinese). Chin J Rock Mech Eng 26(A01):2927–2934

Rupp DE, Selker JS (2006) On the use of the Boussinesq equation for interpreting recession hydrographs from sloping aquifers. Water Resour Res 42(12):W12421

Serrano SE, Workman SR (1998) Modeling transient stream/aquifer interaction with the non-linear Boussinesq equation and its analytical solution. J Hydrol 206(3–4):245–255

Serrano SE (1995) Analytical solutions of the nonlinear groundwater flow equation in unconfined aquifers and the effect of heterogeneity. Water Resour Res 31(11):2733–2742

Shi XQ, Wu JC, Ye SJ, Zhang Y, Xue YQ, Wei ZX, Li QF, Yu J (2008) Regional land subsidence simulation in Su-xi-Chang area and Shanghai City, China. Eng Geol 100(1):27–42

Wang J, Hu L, Wu L, Tang Y, Zhu Y, Yang P (2009) Hydraulic barrier function of the underground continuous concrete wall in the pit of subway station and its optimization. Environ Geol 57(2):447–453

Wang Y, Wong KK, Liu QH, Jin YT, Tu J (2012) Improvement of energy efficiency for an open-loop surface water source heat pump system via optimal design of water-intake. Energ Buildings 51:93–100

Xu YS, Shen SL, Cai ZY, Zhou GY (2008) The state of land subsidence and prediction approaches due to groundwater withdrawal in China. Nat Hazards 45(1):123–135

Xu YS, Ma L, Shen SL, Sun WJ (2012) Evaluation of land subsidence by considering underground structures that penetrate the aquifers of Shanghai, China. Hydrogeol J 20(8):1623–1634

Xu YS, Shen SL, Ren DJ, Wu HN (2016) Factor analysis of land subsidence in Shanghai: a view based on strategic environmental assessment. Sustainability 8(6):573 (1–12)

Xu P, Yu B (2008) Developing a new form of permeability and Kozeny-Carman constant for homogeneous porous media by means of fractal geometry. Adv Water Resour 31(1):74–81

Zeitoun DG, Wakshal E (2013) The subsidence phenomenon throughout the world. In: Land subsidence analysis in urban areas. Springer, Dordrecht, The Netherlands, pp 9–23

Zhang JZ, Huang H, Bi H (2015) Land subsidence in the modern Yellow River Delta based on inSAR time series analysis. Nat Hazards 75(3): 2385–2397

Zhang Y, Wei J, Wang G (2006) Impact of regional groundwater flow on geological temperature field with energy abstraction from the aquifer (in Chinese). J Tsinghua Univ 46(9):1518

Zheng K, Fang H, Wang L (2005) Bacterial growth in a groundwater source heat pump system. J Tsinghua Univ 45(12):1608–1612